# Identifying Linear Vector Fields on 2D Manifolds

Sebastian Volke
Leipzig University, Germany
volke@informatik.uni-leipzig.de

Stefan Koch
Leipzig University, Germany

Mario Hlawitschka
HTWK Leipzig, Germany

## ABSTRACT

Local linearity of vector fields is a property that is well researched and understood. Linear approximation can be used to simplify algorithms or for data reduction. Whereas the concept is easy to implement in 2D and 3D, it loses meaning on manifolds as linearity has either to be defined based on an embedding in a higher-dimensional Cartesian space or on a map. We present an adaptive atlas-based vector field decomposition to solve the problem on manifolds and present its application on synthetic and climate data.

## Keywords

Physical Sciences and Engineering, Environmental Sciences, Vector Field Projection, Vector Field Approximation

## 1 INTRODUCTION

Linear flow behavior in vector fields has been studied, because it allows an easy representation of the flow using the Jacobian matrix, and a characterization in few, well-understood basic linear flow patterns is possible [HSD04]. Investigations of linear vector fields exist for $\mathbb{R}^2$ and $\mathbb{R}^3$, and have proven to be a valuable tool for understanding flow. However, many real-world vector fields—e.g., in the geosciences (convection in the earth mantle), in the oceanic sciences (ocean currents), or in the atmospheric sciences (wind fields)—are tangential vector fields on curved surfaces. These datasets impose difficulties on the analysis, because tangent vectors can not directly be compared and the curvature of the surface has an influence on the vector field direction. Thus, linear flow behavior on manifolds is not directly describable and also not algorithmically accessible.

Usually, manifolds are only investigated at a small scale. One example is the use of cells that subdivide the manifold. A linear interpolation within the cell leads by definition to a linear field. If linearity is defined in the planar projection of each cell, the continuity across cell boundaries is not preserved across cell edges. This has implications, e.g., on the vector field's topology [AH11]. When extending the linearity across larger areas to approximate the field in what has been called a *Affine Linear Neighborhoods* [KWKH13] to describe the field around singularities, special care must be taken to avoid conflicts with the curvature of the surface.

In this paper, we propose a characterization of linear flow behavior on arbitrary two-dimensional manifolds and a method that allows the computation of linear neighborhoods on such manifolds. Based on this, we construct an atlas of the surface together with a corresponding, good linearly approximable, vector field representation. We demonstrate the application of the approach by evaluating synthetic fields on the sphere as well as on a real-world dataset of ocean currents.



## 2 RELATED WORK

The extraction and utilization of local linear vector field approximations has been discussed by several previous works. Schneider et al. [SRWS10] used the linear flow behavior in the vicinity of critical points to improve and accelerate stream surface integration. Wiebel et al. [WKS12] introduced glyphs to investigate the flow behavior at critical points and to study the interaction between them. Later, Koch et al. [KWKH13] introduced the *Affine Linear Neighborhood* (*ALN*). For a particular seed point, an ALN represents all connected points that can be approximated by an affine linear function while staying below a user-defined error threshold. They utilized their ALN definition to present a vector field approximation, as well as a compression, that is based on segmentation [KKW+15].So far, these methods only work on two- or three-dimensional fields but not on curved manifolds.

Other kinds of local approximation are the vector field moments introduced by Bujack et al. [BHSH14]. But there is no extension to arbitrary manifolds, yet. A different approach that lives entirely in the tangential space is the vector field definition using radial basis functions (e.g., Fuselier and Wright [FW09]). Here, the focus is on a reconstruction of the field from sample

points that are scattered on the surface. While this allows to locally characterize the field using kernels, no discussion of linear flow behavior has been done.

# 3 DEFINITION OF LINEARITY

Our goal is an algorithmically usable definition of linearity on manifolds. The main problem is that vectors at different points on the manifold live in different tangent spaces and are not directly comparable. Thus, it is unclear how linearity can be characterized. In the following, we formally define 2D manifolds and vector fields on them. Then, we give two possible definitions of linearity and discuss their applicability. By doing this, we want to make the notion of *"something that looks linear on the manifold"* accessible to computations.

## 3.1 2D Manifolds and Vector Fields

A *differentiable, two-dimensional manifold* $M$ is a topological space that is locally homeomorphic to the two-dimensional Euclidean space. More specifically, it is defined by an *atlas*, i.e., a collection of *charts* $(U_i \subset M, \varphi_i : U_i \to B \subset \mathbb{R}^2)$, such that the $U_i$ are an open cover of $M$ (i.e. $\bigcup_i U_i = M$) and all $\varphi_i$ are homeomorphisms. Furthermore, the chart transitions $\varphi_i \circ \varphi_j^{-1}$ need to be diffeomorphisms.

At each point $p \in M$, we can define a *tangent vector* as an equivalence class of differentiable curves $\gamma : (-\varepsilon, \varepsilon) \in M$ with $\gamma(0) = p$. Thereby, two curves $\gamma_1$ and $\gamma_2$ are equivalent, if and only if $(\varphi \circ \gamma_1)'(0) = (\varphi \circ \gamma_2)'(0)$ for any chart $\varphi$. These vectors form a two-dimensional vector space, the *tangent space* $T_pM$ in $p$. The representation of a tangential vector $v$ in chart $\varphi$ is $(\varphi \circ v)'(0) \in \mathbb{R}^2$.

Note, that the tangent spaces $T_pM$ and $T_qM$ are distinct if $p \neq q$. The union of all tangent spaces forms the *tangent bundle* $TM$ of $M$.

Now, we can define *vector fields* as functions that map a tangent vector to every point of $M$. A vector field $v$ is a function $v : M \to TM$, such that $p \in M \mapsto v(p) \in T_pM$.

## 3.2 Polynomial Vector Fields

Many common two-dimensional manifolds are embeddable into $\mathbb{R}^3$, e.g., the sphere or the surface of mechanical components. Therefore, it is a natural idea to perform all calculations in the space of the embedding and to make use of polynomial vector fields in 3D (cf. [LP06]). A polynomial vector field on the manifold is then a 3D vector field restricted to the manifold that is everywhere tangential to the manifold.

If we can express a 3D vector field in the form of $v(x) = A \cdot x + b$, where $x, b \in \mathbb{R}^3$ and $A \in \mathbb{R}^{3\times 3}$ is the Jacobian matrix, we call it a linear vector field in 3D. Furthermore, we could consider the restriction to the manifold to be a linear vector field. For example, if the manifold is the unit sphere, the field given by $(-y, x, 0)$ would be such a linear polynomial field. However, the surface of some manifolds can not be described by a linear equation. In this case, a field that is linear on a geodesic on the surface may not be a linear polynomial vector field in 3D.

In general we would like to consider a field to be linear, if it has a constant Jacobian on the surface. But, there are two disadvantages with this approach: (1) It is unclear, how a Jacobian on a general manifold is defined. (2) If we simply use Jacobian matrices of the three-dimensional field, it is unclear how to interpret them and how to compare them for different positions of a manifold.

In any case, the Jacobian matrices would need to be transformed into a coordinate reference system that is tangential to the surface. Still, we have one remaining degree of freedom: the rotation around the normal vector of the tangential surface. A meaningful comparison of Jacobian matrices is only possible when consistent alignment is achieved. Therefore, this solution using polynomial vector fields is unsatisfactory for more complex manifolds than planes. Already on the sphere, a globally consistent alignment might be impossible according to the *Hairy ball theorem* [EG79].

## 3.3 Projected Vector Fields

Vectors on the manifold can not directly be compared and thus, linear vector fields can not be easily characterized within $TM$. However, linearity is well defined for vector fields on $\mathbb{R}^n$. We present an approach to describe linearity on 2D manifolds by using a projection of the surface into $\mathbb{R}^2$ and carrying over the vector field into this projection. For this, we assume that an atlas of the manifold is available.

Given a chart $\varphi : M \supset U \to B \subset \mathbb{R}^2, (u_1, u_2) \mapsto (x_1, x_2)$, the tangent space at every point $p \in M$ is characterized by the basis $\left\{ \frac{\partial}{\partial u_1}\Big|_p, \frac{\partial}{\partial u_2}\Big|_p \right\}$. Consequently, the vector field $v : M \to TM$ can be expressed as $v(p) = \sum_{i=1}^{2} a_i(p) \cdot \frac{\partial}{\partial u_i}\Big|_p$. Here, $a_i$ are functions of the form $a_i : U \to \mathbb{R}$ and are called the *coefficients* of the vectors in the chart $\varphi$ [Küh10]. So, for every chart we have a specific representation of the vector field in the form of coefficients. We can analyze these coefficients algorithmically if we find a way to make them comparable across different tangential spaces.

This can be done by moving all vectors into one tangential space by means of a *parallel transport*, i.e. [ZMT06]. In the general case, a computation of the parallel transport is difficult and expensive, as it requires geodesic curves to be integrated.

In this work, we chose a different approach and unify tangential spaces *by projecting them into a common*

*space*. Specifically, we project the basis vectors of each tangential space into $\mathbb{R}^2$ using a chart. The basis vectors $\frac{\partial}{\partial u_1}\Big|_p$ and $\frac{\partial}{\partial u_2}\Big|_p$ are mapped onto the new basis vectors $\left(\frac{\partial x_1}{\partial u_1}\frac{\partial}{\partial x_1} + \frac{\partial x_2}{\partial u_1}\frac{\partial}{\partial x_2}\right)\Big|_{\varphi(p)}$ and $\left(\frac{\partial x_1}{\partial u_2}\frac{\partial}{\partial x_1} + \frac{\partial x_2}{\partial u_2}\frac{\partial}{\partial x_2}\right)\Big|_{\varphi(p)}$. Thus, $\frac{\partial}{\partial x_i}$ corresponds to $\mathbf{e}_i$ in $\mathbb{R}^2$.

Applying this transformation, we obtain a new vector field $\tilde{v}(\tilde{p}) = \sum_{i=1}^{2} a_i(\varphi^{-1}(\tilde{p})) \cdot \left(\frac{\partial x_1}{\partial u_i}\frac{\partial}{\partial x_1} + \frac{\partial x_2}{\partial u_i}\frac{\partial}{\partial x_2}\right)\Big|_{\tilde{p}}$. This vector field is defined on $B \subset \mathbb{R}^2$ and maps into $\mathbb{R}^2$. As the $a_i$ are defined on the manifold, we apply the inverse chart $\varphi^{-1}$ to map from $B$ back onto the manifold to obtain the coefficients.

A disadvantage of this approach are the distortions of the surface that are introduced by the projection. These lead to distortions of the vector field that contradict an intuitive interpretation of the linearity that we observe in the projection. Therefore, in this work, we assume the following requirement to be fulfilled: *As long as the projection of the tangent spaces is sufficiently free of distortions, we can consider $\tilde{v}$ a vector field in planar space that is equivalent to $v$.*

## 3.4 Requirements on projections

In the vicinity of a critical point in two or three-dimensional vector fields, the flow behavior is linear, i.e., the magnitude and orientation of the vector field depends linearly on the distance from the critical point. This behavior is represented by the Jacobian matrix of the critical point. We transfer this concept to manifolds by requiring that the magnitude and orientation of the vector field depends linearly on the geodesic distance from the critical point. Given a critical point on the manifold and a chart of the vicinity of the critical point into $\mathbb{R}^2$. If the chart is sufficiently distortion-free, the projected vector field can be described by the Jacobian at the critical point in $\mathbb{R}^2$. Here, absence of distortion means, that the characteristic flow properties around the critical point are preserved by the projection.

We postulate the following requirements:

1. A linear increase in the vector field magnitudes with increasing distance to the origin (measured along the surface) should be maintained in the chart (measured with Euclidean distance).
2. Geodesic lines that touch the critical point, should be preserved as straight lines in the chart.
3. In a rotational field, particles should rotate around the center at the same frequency independent of the distance to the center, i.e., the angular velocity around the critical point should be preserved.

We designed these requirements so that the typical flow behavior around critical points is preserved by the projection. The first requirement ensures that the typical linear decrease in the vector field magnitudes that can be observed when approaching a critical point, is also present in the projection. The second requirement ensures that, e.g., star sources and sinks appear as such in the projection. The third requirement ensures a correct appearance of the rotating flow around center points.

If a chart satisfies our requirements, linear flow behavior on the manifold is carried over into the projection. Vice versa, linear flow behavior in the projected vector field is also present on the manifold. Thus, linearity on general manifolds becomes computationally accessible.

# 4 APPLICATION TO THE SPHERE

We demonstrate the application of our definition of linear flow behavior by considering the sphere. This two-dimensional manifold has several advantages: It has a well-known embedding into $\mathbb{R}^3$ and many parameterizations and projections into $\mathbb{R}^2$ are available. Furthermore, its constant curvature allows to reliably estimate the effects of the shape of the surface on the projections.

The main task of the application is to choose a projection that is well suited with respect to the requirements stated in the previous section. Because of the curvature of the sphere, it is impossible to meet all three requirements at the same time. For example, requirement 1 and 3 are contradictory. A corollary from the theorem of Gauss-Bonnet is that the perimeter of a circle of radius $r$ deviates from $2\pi \cdot r$ depending on the curvature of the surface. Thus, we either distort the vector magnitudes or the angular velocity [EJ07, Küh10].

Therefore, it is not possible to find a projection that meets all requirements. In the following, we state three common projections and investigate how well they preserve different flow behaviors. Finally, we introduce an approach to deal with the distortions due to the projections by using local charts.

## 4.1 Projections and their Properties

There exists a large variety of projections that preserve different properties in the final map [Sny97]. Especially *conformal* and *equal-area* projections are contrasted. Conformal projections locally preserve angles, respectively shapes. In contrast to this, equal-area projections try to preserve the area measures, which naturally induces distortions.

In the following, we consider the parameterization of the unit sphere in sphere coordinates $(\phi, \lambda)$ with latitude $\phi$ and longitude $\lambda$. A projection is a function $(\phi, \lambda) \mapsto (x, y) \in \mathbb{R}^2$ that directly maps from the parameterization into the plane. If applicable, $(\phi_0, \lambda_0)$ denotes the origin of the projection. We assume the vector field to be given in $(\phi, \lambda)$-coordinates. I.e., for every position $(\phi_{arb}, \lambda_{arb})$ we know the velocity and direction in the tangential space $\left\{\frac{\partial}{\partial\phi}, \frac{\partial}{\partial\lambda}\right\}\Big|_{(\phi_{arb}, \lambda_{arb})}$.

We define the mapped tangential spaces by computing the basis $\left\{\left(\frac{\partial x}{\partial \phi}\frac{\partial}{\partial x}+\frac{\partial y}{\partial \phi}\frac{\partial}{\partial y}\right),\left(\frac{\partial x}{\partial \lambda}\frac{\partial}{\partial x}+\frac{\partial y}{\partial \lambda}\frac{\partial}{\partial y}\right)\right\}$ for the position $(x_{arb}, y_{arb})$. Thus, the projection $\mathbf{v}_{proj}$ of a vector $\mathbf{v}=(v_\phi, v_\lambda)$ is given by

$$\mathbf{v}_{proj}=\begin{pmatrix}\frac{\partial x}{\partial \phi}\cdot v_\phi+\frac{\partial x}{\partial \lambda}\cdot v_\lambda\\ \frac{\partial y}{\partial \phi}\cdot v_\phi+\frac{\partial y}{\partial \lambda}\cdot v_\lambda\end{pmatrix}.$$

To study the flow behavior in projected vector fields, we use the following three projections.

**Orthographic projection –** The *orthographic projection* is given by

$$\begin{aligned} x &= \cos(\phi)\cdot\sin(\lambda-\lambda_0),\\ y &= \cos(\phi_0)\cdot\sin(\phi)-\sin(\phi_0)\cdot\cos(\phi)\cdot\cos(\lambda-\lambda_0).\end{aligned}$$

The corresponding basis vectors are

$$\begin{aligned} \frac{\partial x}{\partial \phi} &= -\sin(y)\cdot\sin(x-x_0),\\ \frac{\partial x}{\partial \lambda} &= \cos(y)\cdot\cos(x-x_0),\\ \frac{\partial y}{\partial \phi} &= \cos(y_0)\cdot\cos(y)\\ &\quad +\sin(y_0)\cdot\sin(y)\cdot\cos(x-x_0),\\ \frac{\partial y}{\partial \lambda} &= \sin(y_0)\cdot\cos(y)\cdot\sin(x-x_0).\end{aligned}$$

It is one of the most common and easiest projections. As shown in Figure 1(b), only the hemisphere facing the tangential plane can be projected. Trivially, it is neither a conformal nor an equal-area projection. Thus, shapes are clearly distorted in the projection and the distortion drastically increases towards the boundaries. However, angular speeds around the map's origin are preserved.

**Mercator projection –** The *Mercator projection* is

$$x=\lambda-\lambda_0,\qquad y=\operatorname{asinh}\big(\tan(\phi)\big).$$

The basis vectors are

$$\begin{aligned} \frac{\partial x}{\partial \phi} &= 0, & \frac{\partial y}{\partial \phi} &= \sqrt{(\cos(y))^{-2}},\\ \frac{\partial x}{\partial \lambda} &= 1, & \frac{\partial y}{\partial \lambda} &= 0.\end{aligned}$$

It was developed by Gerhard Mercator (1512–1594). It maps the sphere to a surrounding cylinder and introduces an appropriated distortion along the cylinder axis to produce a conformal mapping (cf. Figure 1(c)). Thus, small scale geometrical shapes are well preserved. Unfortunately, this projection is not equal-area and the great circles of the sphere are not mapped to straight lines.

**Kavrayskiy VII –** The Kavrayskiy VII projection was introduced by Valdimir Vladimirovich Kavrayskiy (1884–1954). The projection is

$$x=\frac{3}{2}\cdot\lambda\cdot\sqrt{\frac{1}{3}-\left(\frac{\phi}{\pi}\right)^2},\qquad y=\phi.$$

The basis vectors are

$$\begin{aligned} \frac{\partial x}{\partial \phi} &= \frac{-\frac{3}{2}\cdot x\cdot y}{\pi^2\cdot\sqrt{\frac{1}{3}-(\frac{y}{\pi})^2}}, & \frac{\partial y}{\partial \phi} &= 1,\\ \frac{\partial x}{\partial \lambda} &= \frac{3}{2}\cdot\sqrt{\frac{1}{3}-(\frac{y}{\pi})^2}, & \frac{\partial y}{\partial \lambda} &= 0.\end{aligned}$$

It was designed to provide a compromise between a perfect equal-area and conformal projection. The obtained map exhibits only small overall distortions (cf. Figure 1(d)). Thus, the Kavrayskiy VII projection is a good candidate for general purposes and is the last mapping we use for our study.

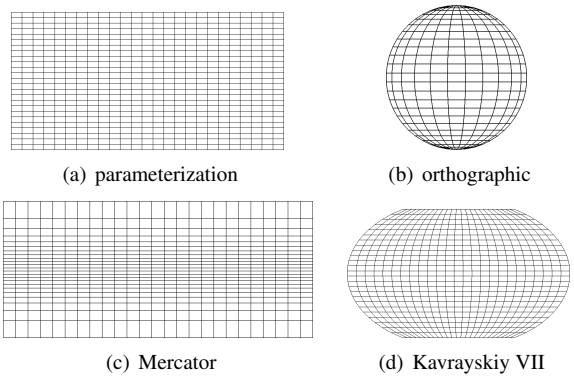

(a) parameterization (b) orthographic (c) Mercator (d) Kavrayskiy VII

Figure 1: Figure 1(a) shows the parameterized grid of a sphere and 1(b) to 1(d) its projected counterparts. While the orthographic projection nicely represent the sphere's shape, it unfortunately discards one hemisphere. The other two projections realize a conformal (cf. 1(c)), and a compromise between equal-area and conformal projection (cf. 1(d)).

## 4.2 Atlas-Based Decomposition

The distortion caused by a projection commonly increases with the distance from the map's origin. Thus, linear flow behavior on a sphere, as defined in Section 3.4, usually can not be preserved globally in a projection. This triggers the natural idea to use several charts that only project small parts of the manifold.

By using multiple charts that locally project the vector field into $\mathbb{R}^2$, we obtain an *atlas-based representation* of the vector field. The construction of the atlas has to ensure that the obtained vector field projections are almost distortion-free. For example, one could use every critical point of the sphere's vector field as the projection center for one chart to preserve the flow behavior in its vicinity as good as possible.

Furthermore, we can generalize the approach of local projections to non-critical points. Then, the charts can be based on regions on the manifold with mostly affine linear flow behavior in order to obtain a simple and easy comprehensible representations of the vector field. This idea corresponds to the work of Koch et

al. [KWKH13, KKW+15], who determined regions of mainly linear flow behavior in vector fields.

## 5 RESULTS

We demonstrate the influence of projections on the representation of linear flow behavior on manifolds by considering Affine Linear Neighborhoods (ALNs). Generally, an ALN is defined as

$$L_{\mathbf{x}_s} = \left\{ \mathbf{y} \in \mathbb{R}^3 \,\middle|\, \|\mathbf{v}(\mathbf{y}) - J_{\mathbf{x}_s} \cdot (\mathbf{y} - \mathbf{x}_s) - \mathbf{v}(\mathbf{x}_s)\| < E_{max} \right\}.$$

For a seed point $\mathbf{x}_s$, the ALN represents the set of positions that can be approximated by the linear vector field that is given by the Jacobian $J_{\mathbf{x}_s}$ and the offset vector $\mathbf{v}(\mathbf{x}_s)$, while staying below a specific approximation error $E_{max}$. In the case of vector fields on manifolds, we consider these approximations in the local charts, as described in Section 4.2. Thus, we can infer the extension of the linearly describable flow on the manifold by mapping back all positions of the ALN in the projection.

### 5.1 Synthetic Vector Field

To evaluate the requirements on projections of Section 3.4, we designed different synthetic datasets. These fields show different types of linear flow behavior. This allows us to study the impact of the projection on all three requirements separately.

Since the orthographic projection is very common and the effects of this projection are clearly visible, we first limit our considerations to this projection type, before introducing the results of the proposed atlas-based vector field decomposition (cf. Section 4.2).

**Constant Tangential Vector Field –** To investigate the influence of the projection on the flow magnitudes, we generate two constant, tangential vector fields. One field is tangent to the circles of latitude

$$\mathbf{v}(\mathbf{s}) = \begin{pmatrix} \frac{1}{\cos(\lambda)} \\ 0 \end{pmatrix} \tag{1}$$

and one tangential to the lines of longitudes

$$\mathbf{v}(\mathbf{s}) = \begin{pmatrix} 0 \\ -1 \end{pmatrix}, \tag{2}$$

with $\mathbf{s} = (\phi, \lambda)$, $\phi \in [-\pi, \pi)$, and $\lambda \in [-\frac{\pi}{2}, \frac{\pi}{2}]$. The factor $\frac{1}{\cos(\lambda)}$ compensates the non-linear magnitude changes due to the decreasing radii of the circles of latitude towards the poles.

The parts of the vectors that point into the viewing direction of the projection will vanish and cause visible magnitude changes. This is clearly observable in Figures 2(a) and 2(d). If all vectors are parallel to the projection plane, the vectors will not be changed due to the projection. This is shown in Figure 2(b). Here, only the discontinuity in the pole stands out.

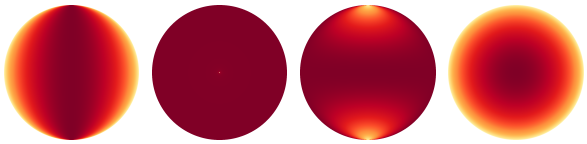

(a) lat. (side) (b) lat. (top) (c) long. (side) (d) long. (top)

Figure 2: These color maps show the magnitude changes of two constant, tangential vector fields due to the orthographic projection (cf. Equations 1 and 2). Figure 2(a) shows the field tangential to the circle of latitudes with the projection center in $(0,0)$ and 2(b) with the projection center $(0, \frac{\pi}{2})$. Figures 2(c) and 2(d) analogously show the field tangential to the lines of longitude. The used color map depicts vectors with a magnitude of one in dark red and zero vectors in white.

**Linear Vector Field –** According to requirement 1 in Section 3.4, we generate two further synthetic vector fields where the vector magnitudes increase linearly with the geodesic distance from the north pole. One field has a *center* point

$$\mathbf{v}(\mathbf{s}) = \begin{pmatrix} (\frac{\pi}{2} - |\lambda|) \cdot \frac{1}{\cos(\lambda)} \\ 0 \end{pmatrix} \tag{3}$$

and one has a *source* in the north pole of the sphere

$$\mathbf{v}(\mathbf{s}) = \begin{pmatrix} 0 \\ -\frac{\pi}{2} - |\lambda| \end{pmatrix}. \tag{4}$$

Additionally to the factor $\frac{1}{\cos(\lambda)}$, described in the previous paragraph, the factor $(\frac{\pi}{2} - |\lambda|)$ incorporates the distance from the north pole along a fixed line of longitude. It causes a linear increase of the vector magnitudes with increasing distance from the pole.

Please note, requirement 3 can not be satisfied by this field design. The radii of circles of latitude grow slower than linear with the geodesic distance to the pole. Thus, a linear increase in vector magnitudes also leads to an increase in angular speed around the pole. The projections that we use here can not compensate this.

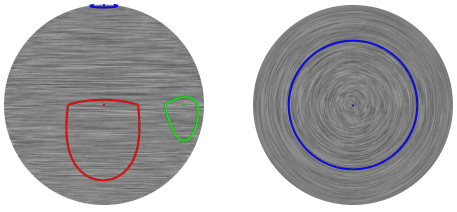

(a) $\mathbf{x}_{mc} = (0,0)$ (b) $\mathbf{x}_{mc} = (0, \frac{\pi}{2})$

Figure 3: These LIC images show the center field described by Equation 3. The depicted regions are ALNs seeded in $(0,0)$ (red), $(0.8 \cdot \pi, 0)$ (green), and $(0, \frac{\pi}{2})$ (blue). For each ALN, $E_{max} = 0.1$ was used.

Figure 3 shows two *Line Integral Convolution* [SH95] (*LIC*) images of the center point field. When the projection center is on the equator of the sphere (Figure 3(a)),

the magnitudes of the tangential vector field approach zero towards the boundary of the projection. Thus, the flow behavior gets more and more non-linear towards the boundary. This is demonstrated by the differently seeded ALNs. When the projection center is at the north pole (Figure 3(b)), the tangential vectors are parallel to the projection plane and the change in vector magnitude is only due to the lengthening along the circles of latitude. The flow directions and angular speed around the center point are preserved in this top-view.

Summarizing, we are only able to approximate small regions by a linear function. One can clearly see by Figure 3(a) that the extracted ALNs get smaller and smaller towards the projection's domain boundary. These distortion can be minimized by using a map, where the map center is also the ALN seed point (cf. Figure 3(b)).

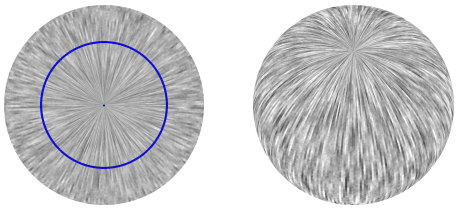

(a) $\mathbf{x}_{mc} = (0, \frac{\pi}{2})$ (b) $\mathbf{x}_{mc} = (0, 1)$

Figure 4: Analogously to Figure 3(b), the left image shows the source field of Equation 4 with an ALN ($E_{max} = 0.1$) seeded in $(0, \frac{\pi}{2})$. The right image shows the same field projected with $(0, 1)$ as the map center.

Figure 4 shows LIC images of the second synthetic vector field, the source field. Analogously to Figure 3(a), the projected vector field approaches zero towards the boundary. Again, the non-linear magnitude change due to the projection and the scaling of the field along the lines of longitude have the effect that the projected field can not be completely described by a affine linear field in the projection. But if the critical point is located directly in the map center, all geodesic curves that touch it are mapped to straight lines. Thus, requirement 2 is satisfied. Figure 3(b) shows the corresponding counterexample when the critical point is further away from the map center. Here the non-linearity of the projection causes a qualitatively different course of the streamline.

To summarize our first findings, only a region around the map center is sufficiently distortion-free, so that realistic analysis results can be obtained. Thus, we think that it is necessary to use an approach like the proposed atlas-based vector field decomposition for the analysis of linear flow behavior on spheres.

For the comparison of different projection types, we considered the source field (Equation 4). The projected vector fields were segmented into regions that can be linearly approximated without exceeding a specific approximation error. For this, we used the segmentation

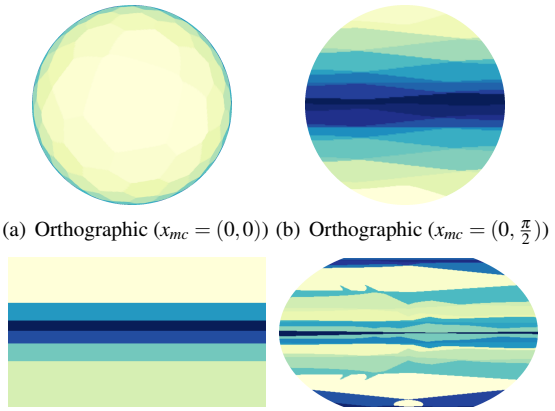

(a) Orthographic ($x_{mc} = (0,0)$) (b) Orthographic ($x_{mc} = (0, \frac{\pi}{2})$)

(c) Mercator (d) Kavrayskiy VII

Figure 5: Segmentation using the algorithm of Koch et al. [KKW+15]. The color map shows the seeding order of the segments from white to blue. Figure 5(a) shows 127, 5(b) 20, 5(c) 6, and 5(d) 24 segments.

algorithm of Koch et al. [KKW+15]. Their method decomposes a vector field into regions that are at least ALN subsets. To allow the extraction of the best and largest regions with a linear flow behavior, a heuristic based on the field's derivatives is used to predict the needed ALN seed points. The ALN-computation is iteratively applied until all positions in the field are assigned to at least one ALN. If the assignment of a point to the ALNs is not unambiguous during this iterative process, it gets assigned to that ALN, which approximates the corresponding vector value best.

The resulting segmentations reveal which parts of the projections can be used for a realistic representation of the vector field, similar to the ALNs that we discussed above. Figure 5 shows the segmentation results for the different projection types. The orthographic projection generates the largest linearly approximable region around the critical point, when the critical point is also the map center (Figure 5(a)). However, because of the distortions towards the projection boundary, this projection also generates the most segmentation regions. When the map center is at the equator (Figure 5(b)), a moderate number of segments is created. The best approximations can be achieved near the poles and the sizes of the segments slightly decrease towards the map center here. The Mercator projection (Figure 5(c)) produces the fewest segments and very large regions around the poles that can be well linearly approximated. This is a result from the conformality of this projection, since the preservation of angles has a great impact on the distortion of the vector magnitudes here. The Kavrayskiy VII projection (Figure 5(d)) is not conformal and leads to more and smaller segments, i.e. a smaller part of the projection has a meaningful interpretation. Still, fewer segments are created than in the case of the orthographic projection.

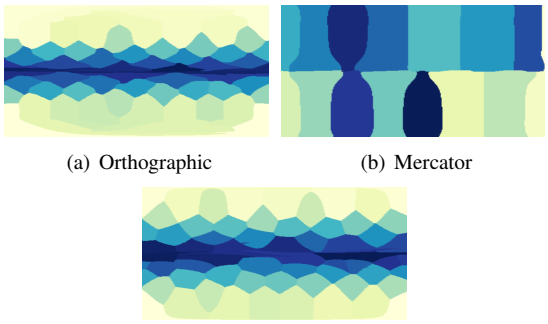

(a) Orthographic (b) Mercator

(c) Kavrayskiy VII

Figure 6: Atlas-based vector field decomposition of the source field in the $(\phi, \lambda)$-parameter space. Each region can be well linearly approximated and corresponds to one chart of the atlas. Figure 6(a) shows 55, 6(b) 16, 6(c) 61 regions. The small number of regions can be obtained due to the absence of high distortions that occur in the different projections.

In sum, the Mercator projection appears to represent the linear vector fields best in this synthetic example. The orthographic projection is worst, depending whether the map center is aligned with the critical point or not.

**Atlas-based Vector Field Decomposition –** To demonstrate the construction of an atlas-based vector field decomposition, we again use the segmentation algorithm of Koch et al. [KKW+15] and adapt it to the sphere. For every seed point candidate, the vector field is projected into $\mathbb{R}^2$ while keeping the seed point at the map center. Thus, the heuristic of the original algorithm can be applied to the projected field to predict the region with the most linear flow behavior. For the found seed point, an ALN is computed in the projection to determine the extension of the new chart of the desired atlas. This process is applied iteratively until the complete field is segmented. Because the original algorithm was designed to compute the largest possible regions, the number of charts of the atlas should be minimal.

On the example of the source field (Equation 4), we compare the results for different projection types. Figure 6 shows the results. There is only a small difference between the Kavrayskiy VII projection and the orthographic projection. In both cases, many charts are needed, especially near the equator. The Mercator projection results in the simplest atlas, consisting of only 16 charts. This shows again, that the conformality, i.e., the preservation of angles in the projection, is very beneficial for the analysis of this synthetic example.

## 5.2 Real-World Example

To provide a real-world example, we consider the ocean currents of the whole world in six meter depth. This dataset consists of 8 618 400 grid positions.

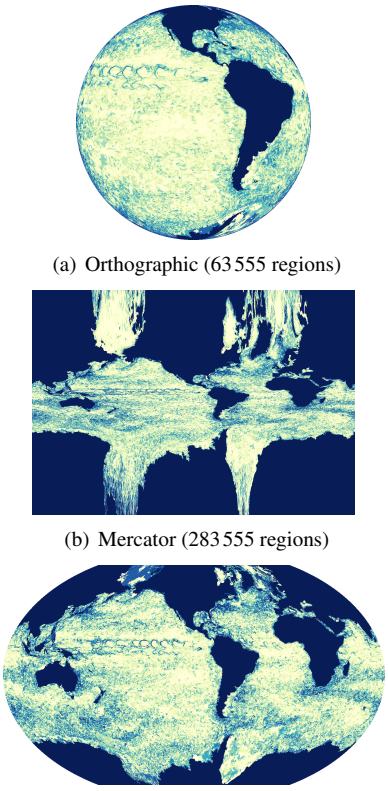

(a) Orthographic (63 555 regions)

(b) Mercator (283 555 regions)

(c) Kavrayskiy VII (180 978 regions)

Figure 7: Segmentation of Koch et al. [KKW+15] ($E_{max} = 10^{-4}$), applied to projections of the ocean currents. It shows a high number of approximated regions and high distortions of the shapes of the continents.

When looking at the naïve segmentation of this dataset in Figure 7, we see the same shortcomings as in the synthetic fields. For example, the orthographic projection again produces a very high number of segments, due to the high non-linearity towards the domain boundary. The high distortions of shapes on the sphere are also visible in the projections (cf. Australia in Figure 7(b)). Furthermore, from the previous section, we know that the linear regions in these projections are non-realistic.

The results of the atlas-based vector field decomposition are very similar. That is why we only show the example of the orthographic projection in Figure 8, Nevertheless, we know that the Kavrayskiy VII already introduces vector field distortions at the map center. That is why, we do not recommend this projection for our approach. In contrast to the first results, both, the orthographic, as well as the Mercator projection, provide good results here. Since the flow is very turbulent, the linearly approximable charts are mostly small in size and therefore satisfy our requirements on projected linear flow behavior very well in vicinity of the corresponding map centers.

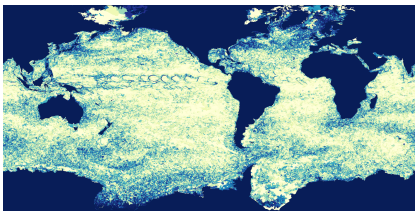

Figure 8: Atlas of the ocean currents using an orthographic projection for the vector field decomposition. The atlas contains 204 659 charts. Because of the complex structures in the flow, the charts are relatively small and therefore sufficiently distortion free.

## 6 CONCLUSION AND FUTURE WORK

Characterizing linearity on general 2D manifolds is a difficult problem, because tangent vectors at different points of the manifold can not directly be compared against each other. We propose a local representation of vector fields in $\mathbb{R}^2$ using projections. For this, we unify the tangent spaces at different points on the manifold by projecting them into a common space, in this case into the $\mathbb{R}^2$. Our proposed requirements on the projection ensure the preservation of certain properties of the original vector fields that are important for characterizing linear flow behavior. The projected field is accessible to known analysis methods and can be investigated as a substitute of the original field on the manifold.

The concept is evaluated on the example of the sphere. We compare different projection types regarding their suitability according to the requirements. A decomposition of the vector field into multiple charts, that are each sufficiently free of distortions and together represent the whole vector field, is proposed and demonstrated for both, synthetic examples of simple linear vector fields, as well as a real world example of ocean currents.

This is only a first step to investigate linearity on 2D manifolds. Future work can improve the way the tangent spaces are unified, evaluate the influence of changes in curvature on the quality of the projection, and also construct a design space of projection techniques that allows to choose the best possible projection for the analysis task at hand.

## 7 ACKNOWLEDGMENTS

Special thanks go to the *FAnToM* development group for providing the visualization software and the working environment. Furthermore, we thank James Ahrens for the access to the climate datasets via ESG-NCAR. The first two authors contributed equally to this work.

## 8 REFERENCES

[AH11] C. Auer and I. Hotz, Complete tensor field topology on 2d triangulated manifolds embedded in 3d, In CGF, vol. 30, pg. 831–840, 2011.

[BHSH14] R. Bujack, I. Hotz, G. Scheuermann, and E. Hitzer, Moment invariants for 2d flow fields using normalization, In IEEE PacificVis 2014, pg. 41–48, 2014.

[EG79] M. Eisenberg and R. Guy, A proof of the hairy ball theorem, Am. Mathematical Monthly, pg. 571–574, 1979.

[EJ07] J.-H. Eschenburg and J. Jost, Differentialgeometrie und Minimalflächen, Springer, 2007.

[FW09] E.-J. Fuselier and G. Wright, Stability and error estimates for vector field interpolation and decomposition on the sphere with rbfs, SIAM Journal on Numerical Analysis, vol. 47(5), pg. 3213–3239, 2009.

[Hal01] G. Haller, Lagrangian structures and the rate of strain in a partition of two-dimensional turbulence, Physics of Fluids (1994-present), vol. 13(11), pg. 3365–3385, 2001.

[HSD04] M.-W. Hirsch, S. Smale, and R.-L. Devaney, Differential Equations, Dynamical Systems, and an Introduction to Chaos, vol. 60, Academic Press, 2004.

[KKW+15] S. Koch, J. Kasten, A. Wiebel, G. Scheuermann, and M. Hlawitschka, 2d vector field approximation using linear neighborhoods, The Visual Computer, 2015.

[KWKH13] S. Koch, A. Wiebel, J. Kasten, and M. Hlawitschka, Visualizing linear neighborhoods in non-linear vector fields, In IEEE PacificVis 2013, pg. 249–256, 2013.

[Küh10] W. Kühnel, Differentialgeometrie, Springer, 2010.

[LP06] J. Llibre and C. Pessoa, Homogeneous polynomial vector fields of degree 2 on the 2-dimensional sphere, Extracta Mathematicae, vol. 21(2), pg. 167–190, 2006.

[SRWS10] D. Schneider, W. Reich, A. Wiebel, and G. Scheuermann, Topology aware stream surfaces, CGF, vol. 29(3), pg. 1153–1161, 2010.

[Sny97] J.-P. Snyder, Flattening the earth: two thousand years of map projections, University of Chicago Press, 1997.

[SH95] D. Stalling and H.-C. Hege, Fast and resolution-independent line integral convolution, In SIGGRAPH '95, pg. 249–256, 1995.

[WKS12] A. Wiebel, S. Koch, and G. Scheuermann, Glyphs for non-linear vector field singularities, In TopoInVis Workshop 2011, pg. 177–190. Springer, 2012.

[ZMT06] E. Zhang, K. Mischaikow, and Greg Turk, Vector field design on surfaces, ACM Transactions on Graphics, vol. 25(4):, pg. 1294–1326, 2006.